Cichocki, F., Merino, M., and Ahedo, E. (2020). Three-dimensional geomagnetic field effects on a plasma thruster plume expansion. In Acta Astronautica (Vol. 175, pp. 190–203).

DOI: https://doi.org/10.1016/j.actaastro.2020.05.019

Contents lists available at ScienceDirect

Acta Astronautica

journal homepage: http://ees.elsevier.com

Three-dimensional geomagnetic field effects on a plasma thruster plume expansion

F. Cichocki *, M. Merino, E. Ahedo

Equipo de Propulsión Espacial y Plasmas, Universidad Carlos III de Madrid, Leganés, Spain

ABSTRACT

A 3D hybrid particle-in-cell code with a partially-magnetized fluid electron model is presented and applied to study the effects of a uniform external geomagnetic field on an expanding plasma thruster plume at three different angles. Electron currents are governed by both the magnetic field and collisional effects with the heavy ions and neutrals. While an axial magnetic field (parallel to the plume axis) induces azimuthal electric currents and an observable plume channeling, an oblique field produces non-trivial asymmetric deformations of the plume cross-section, and induces axial-radial electric current loops. A center of mass analysis of the plasma plume demonstrates that the electron response produces an electric field that balances the Lorentz force deflection on the ions, so that no net plume momentum deflection is observed.

1. Introduction

The complex interaction between an expanding plasma thruster plume and the emitting spacecraft is a topic of great interest in the plasma propulsion community. In fact, it is crucial for satellite integration, in which the impact of the plasma plume on sensitive surfaces (including both sputtering and contamination) has to be minimized [1]. Such interaction is of fundamental importance also in the context of the Ion Beam Shepherd [2–4], a space debris removal technique, where a target object is relocated to a different orbit by means of the ion push of a plasma thruster plume directed towards it.

In these contexts, the presence of a background magnetic field, like the geomagnetic one, further complicates the physics of the jet. In fact, a magnetized plasma plume expands differently into vacuum compared to an unmagnetized one, and hence its interaction with the satellite or with any downstream object is clearly affected. For the typical geomagnetic field magnitude (fractions of Gauss), only the electrons are magnetized, while the heavy ions present gyro-radii that are much larger than the plume characteristic size. It is the consequent change in electron anisotropic mobility with respect to the unmagnetized scenario that produces different ambipolar electric fields and hence a different plume expansion. These changes depend on both the field intensity and direction, as suggested by Korsun et al. [5,6], who indicated plasma plume channeling for a magnetic field aligned with the plume axis, and an asymmetric distortion of the plume cross section for oblique fields (i.e. at an angle with the plume axis). While the latter effect is non-trivial, the former channeling effect can be easily explained with the reduction in the radial mobility of the electrons that is induced by an axial magnetic field. This produces a lower (compared with the unmagnetized case) radial electric field and hence a lower divergence. However, apart from Korsun's work, no similar studies have been found in the literature to confirm and extend these findings, so that this research field remains particularly open.

The large amount of plasma plume codes developed in recent years [6–27] demonstrates a clearly increasing interest in plume expansion and S/C interaction studies. Nevertheless, out of the existing codes, only a few of them deal with magnetized plume expansions. Korsun et al. in Ref. [6] describe a magnetized fluid model based on an approximate three-dimensional self-similar expansion, and discuss the magnetic field effects mentioned above. Taccogna, in Ref. [22], considers a computationally demanding 3D particle-in-cell (PIC) model for both ions and electrons to simulate the discharge and the near-plume of a Hall Effect thruster. Finally, several codes have been developed for the axisymmetric two-dimensional simulation of Hall effect thrusters discharge and near-plume, based on either a multi-fluid [10] or a hybrid approach [26,27] (heavy species treated as particles and electrons as a fluid). To the authors' knowledge, however, no hybrid particle-in-cell/fluid code exists that can deal with a three-dimensional magnetized far-region plume expansion.

In order to tackle the main goal of the paper and perform an analysis of a far plume expansion under the effect of the geomagnetic field, an existing in-house 3D hybrid code, named EP2PLUS (Extensible Parallel Plasma PLUme Simulator) has been upgraded to include the effects of a mild external and uniform magnetic field. This code makes use of a non-uniform structured grid for both the PIC and electron models. The former is in charge of computing the bulk properties associated to both ions and neutrals (e.g. number densities and fluxes). The latter, taking this data as input, solves for both the electron proper-

* Corresponding author.
E-mail address: filippo.cichocki@uc3m.es (F. Cichocki)

https://doi.org/10.1016/j.actaastro.2020.05.019
Received 21 February 2020; Received in revised form 24 April 2020; Accepted 9 May 2020
Available online xxx
0094-5765/

ties and the electric field required by the PIC model, by assuming an electron closure relation, which can be an isotropic barotropy relation, such as a polytropic law, or a more advanced model based on the output of fully-kinetic electron codes [19]. The original version of the electron model, by retaining collisional effects, already solved for a thermalized potential (whose gradient represents a net total force on the electrons), being capable of computing the electron current density in the plume of an NSTAR thruster [23].

In this work, EP2PLUS is applied to a set of simulations featuring different angles between a uniform background magnetic field and the axis of the plasma plume. By comparing these magnetized plume expansions with that of an unmagnetized scenario, the effects of the magnetic field are evaluated in terms of induced electric fields, electric currents, plasma plume deformation and deviation.

The rest of the paper is structured as follows. The PIC model for the ions is summarized in Sec.2. The magnetized electron fluid model is described in Sec. 3. The simulation results for different applied magnetic field orientations are reported and discussed in Sec. 4. Finally, conclusions are summarized in Sec. 5, and two appendices discuss the effects of certain modeling assumptions.

2. The particle-in-cell model

In EP2PLUS, the PIC model is in charge of simulating the heavy species particles (ions and neutrals) and is fully described in Ref. [23]. In the following, we provide only a short summary of its main algorithms. As in all PIC approaches, the heavy particles distribution function is discretized in the position-velocity phase-space with a given number of macro-particles, each representing W_j elementary particles and having position $\boldsymbol{r}_j$. The bulk properties, like number density, fluid velocity and temperature, are then obtained by weighting these macro-particles to the nodes of a structured non-uniform mesh [28], further described in Sec. 4.1. For each time step Δt, the PIC model performs operations such as: *(i)* moving the macro-particles according to Newton's law, that is, for the j^{th} macro-particle:

$$m_j \frac{\mathrm{d}\boldsymbol{v}_j}{\mathrm{dt}} = eZ_j \left[\boldsymbol{E}\left(\boldsymbol{r}_j\right) + \boldsymbol{v}_j \times \boldsymbol{B}\left(\boldsymbol{r}_j\right)\right], \tag{1}$$

where $\boldsymbol{E} = -\nabla\varphi$ and $\boldsymbol{B}$ are the electric and magnetic fields at the macro-particle position, $\boldsymbol{v}_j$ is the macro-particle velocity, and m_j, Z_j are respectively the elementary mass and charge number of the heavy species population (e.g. $Z_j = 1$ for singly-charged ions); *(ii)* injecting new macro-particles into the simulation domain from the injection boundary (targeting a given number of macro-particles per cell); *(iii)* eliminating macro-particles that exit the simulation domain; *(iv)* performing collisions between macro-particles; and *(v)* weighting the macro-particles to the mesh nodes to obtain their fluid bulk properties (used by the electron model).

In order to better illustrate the magnetic field effects on the plume expansion, in this paper we only consider one species of ions, and we neglect collisional effects on their dynamics (nearly collisionless plasma plume). As shown in Sec. 4.1, the neutrals are considered as a uniform and still background, and only for the purpose of computing electron-neutral collisions. The effects of such a uniform background of neutrals are discussed in detail in Appendix B.

3. The magnetized electron model

The electron model presented here is the generalization of the one introduced in Ref. [23] to include magnetization effects. For an electron fluid of negligible inertia, the electron momentum equation can be written as:

$$0 = -\nabla\cdot\mathscr{P}_\mathrm{e} - en_\mathrm{e}\left(\boldsymbol{E} + \boldsymbol{u}_\mathrm{e}\times\boldsymbol{B}\right) - \sum_s \nu_{\mathrm{e}s} m_\mathrm{e} n_\mathrm{e}\left(\boldsymbol{u}_\mathrm{e} - \boldsymbol{u}_s\right) \tag{2}$$

where $\mathscr{P}_\mathrm{e}$ is the electron pressure tensor, n_e is the electron number density, m_e is the electron mass, $\boldsymbol{u}_\mathrm{e}$ is the electron fluid velocity, the summation term extends to all heavy particles populations (with which the electrons undergo momentum-exchange collisional processes), and $\nu_{\mathrm{e}s}$ is the effective momentum transfer collision frequency of the electrons with the s^{th} heavy population, which features a fluid velocity $\boldsymbol{u}_s$ (refer to Ref. [23] for the models considered for $\nu_{\mathrm{e}s}$).

Under the assumption that the pressure tensor is diagonal and isotropic, that is $\nabla\cdot\mathscr{P}_\mathrm{e} = \nabla p_\mathrm{e}$, and that the electron closure is barotropic, that is $p_\mathrm{e} \equiv p_\mathrm{e}\left(n_\mathrm{e}\right)$, a barotropy state function h_e is introduced, such that $\nabla h_\mathrm{e} = \nabla p_\mathrm{e}/n_\mathrm{e}$ is an exact differential. In the following, an isothermal electron fluid closure (special cases of barotropy) is further assumed, so that:

$$h_e\left(n_e\right) = T_{e0}\ln\left(\frac{n_e}{n_{e0}}\right), \tag{3}$$

where $n_{\mathrm{e}0}$, $T_{\mathrm{e}0}$ are the reference electron density and temperature where $h_\mathrm{e} = 0$. A polytropic closure is also available, as described in Ref. [23].

Let us define: $\boldsymbol{j}_\mathrm{e} = -en_\mathrm{e}\boldsymbol{u}_\mathrm{e}$ and $\boldsymbol{j}_\mathrm{i} = e\sum_s Z_s n_s \boldsymbol{u}_s$ the electron and ion current densities (Z_s and n_s are respectively the charge number and the number density of the generic s^{th} heavy particle population); $\nu_e = \sum_s \nu_{\mathrm{e}s}$ the total electron momentum transfer collision frequency; and

$$\boldsymbol{j}_\mathrm{c} = \frac{en_\mathrm{e}}{\nu_\mathrm{e}}\sum_s \nu_{\mathrm{e}s}\boldsymbol{u}_s \tag{4}$$

an effective current density grouping collisional effects from heavy species. Then, the electron momentum equation becomes

$$0 = en_\mathrm{e}\nabla\varphi - n_e\nabla h_e + \boldsymbol{j}_\mathrm{e}\times\boldsymbol{B} + \frac{m_\mathrm{e}\nu_\mathrm{e}}{e}\left(\boldsymbol{j}_\mathrm{e} + \boldsymbol{j}_\mathrm{c}\right). \tag{5}$$

For the rarefied plasmas of interest here, the first two terms on the right hand side (pressure and electric forces) are often dominant, in magnitude, and they almost compensate each other, so it is convenient to define the residual 'thermalized potential' Φ, such that $\nabla\Phi = \nabla\varphi - \nabla h_\mathrm{e}/e$. Assuming the same reference zero point for Φ, h_e and φ yields

$$\Phi = \varphi - \frac{h_e}{e}. \tag{6}$$

Note that the electron Bernoulli energy function H_e of Ref. [23] is just $H_\mathrm{e} = -e\Phi$. In terms of Φ, Eq. (5) becomes:

$$0 = en_\mathrm{e}\nabla\Phi + \boldsymbol{j}_\mathrm{e}\times\boldsymbol{B} + \frac{m_\mathrm{e}\nu_\mathrm{e}}{e}\left(\boldsymbol{j}_\mathrm{e} + \boldsymbol{j}_\mathrm{c}\right) \tag{7}$$

In the unmagnetized ($\boldsymbol{B} = 0$), collisionless ($\nu_e = 0$) limit, this equation yields simply $\Phi = 0$ and thus the electric potential satisfies identically the Boltzmann relation $e\varphi = h_\mathrm{e} = T_{\mathrm{e}0}\ln\left(n_\mathrm{e}/n_{\mathrm{e}0}\right)$, for isothermal electrons. The gradient of the thermalized potential Φ measures the correction to that relation due to the magnetic and resistive forces. Therefore, it is the net force shaping the electron response and determining the electron current density. For a finite non-zero total collision frequency ($\nu_\mathrm{e}>0$), solving Eq. (7) for $\boldsymbol{j}_\mathrm{e}$ yields the generalized electron Ohm's law

$$\boldsymbol{j}_\mathrm{e} = -\mathscr{K}\cdot\left(\sigma_\mathrm{e}\nabla\Phi + \boldsymbol{j}_\mathrm{c}\right), \tag{8}$$

where $\sigma_\mathrm{e} = e^2 n_\mathrm{e}/\left(m_\mathrm{e}\nu_\mathrm{e}\right)$ is the scalar electron conductivity,

$$\mathscr{K} = \begin{bmatrix} 1 & \chi b_\mathrm{z} & -\chi b_\mathrm{y} \\ -\chi b_\mathrm{z} & 1 & \chi b_\mathrm{x} \\ \chi b_\mathrm{y} & -\chi b_\mathrm{x} & 1 \end{bmatrix}^{-1} \tag{9}$$

is the normalized conductivity tensor, $\boldsymbol{1}_\mathrm{b} = \left(b_\mathrm{x}, b_\mathrm{y}, b_\mathrm{z}\right)$ is the unit vector along $\boldsymbol{B}$, and $\chi = eB/\left(m_e\nu_\mathrm{e}\right)$ is the Hall parameter.

In steady-state (or even during transients for quasineutral simulations), the total current density $\boldsymbol{j} = \boldsymbol{j}_\mathrm{e} + \boldsymbol{j}_\mathrm{i}$ satisfies the continuity equa-

tion

$$\nabla \cdot \boldsymbol{j} = 0. \tag{10}$$

Substituting here Eq. (8) for $\boldsymbol{j}_e$ yields an elliptic equation for Φ, i.e.:

$$\mathscr{K} : \nabla\nabla\Phi + \nabla\Phi\cdot(\nabla\cdot\mathscr{K}) + \mathscr{K}\cdot\nabla\Phi\cdot\nabla \ln \sigma_e = \frac{\nabla\cdot(\boldsymbol{j}_i - \mathscr{K}\cdot\boldsymbol{j}_c)}{\sigma_e} \tag{11}$$

where $\nabla\nabla\Phi$ is the Hessian tensor of Φ and the operator $:$ represents a tensor contraction. In the unmagnetized case $\chi \to 0$, and $\mathscr{K}$ tends to the identity tensor, so Eq. (11) becomes the unmagnetized elliptic equation that was already discussed in Ref. [23]:

$$\nabla^2\Phi + \nabla\Phi\cdot\nabla \ln(\sigma_e) = \frac{\nabla\cdot(\boldsymbol{j}_i - \boldsymbol{j}_c)}{\sigma_e}. \tag{12}$$

The presented model can be used in both quasineutral and non-neutral (quasi) steady-state simulations. While in the former, both $n_e = \sum_s Z_s n_s$ and hence σ_e are functions of the heavy species properties, in the latter non-neutral case, Eq. (11) can be solved using the previous time step values of n_e and σ_e, which are now obtained by solving a non-linear Poisson's equation [23]. Since the focus is on magnetic field effects on the electrons, in this study the plasma is assumed to be quasineutral everywhere, and Poisson's equation is not considered.

3.1. Boundary conditions

Solving Eq. (11) requires prescribing the value of Φ at an arbitrary point in the domain (e.g. at the reference point for the electric potential), and either its value or directional derivative at the simulation boundaries. In this work, for simplicity, we will impose a boundary condition directly on the electric current density, which is equivalent to imposing the directional derivative of the thermalized potential.

In fact, if $\mathbf{1}_n$ is the normal unit vector at the boundaries, directed inwards towards the simulation domain, the imposition of a prescribed normal electric current density is equivalent to stating:

$$\sigma_e(\mathscr{K}\cdot\nabla\Phi)\cdot\mathbf{1}_n = (\boldsymbol{j}_i - \mathscr{K}\cdot\boldsymbol{j}_c)\cdot\mathbf{1}_n - j_n, \tag{13}$$

where $j_n = (\boldsymbol{j}_e + \boldsymbol{j}_i)\cdot\mathbf{1}_n$ is the local normal electric current density at the boundary. Eq. (13) imposes the directional derivative of Φ along the direction $\mathscr{K}^T\cdot\mathbf{1}_n$, which is generally different from the boundary normal direction (but tends to it when $B \to 0$ or if $\mathbf{1}_b \to \mathbf{1}_n$).

In stationary conditions, the Gauss's theorem applied to Eq. (10) urges that the integrated current through the simulation boundary be identically zero. However, the local value of j_n at the boundary satisfying this integral relation cannot be known a priori, except at known regions of the plasma plume, like the injection plane where we know the plume conditions in terms of electric current (e.g. an initially current-free plasma plume, a condition that is approached in a relatively short distance from the exhaust section, for the majority of plasma thrusters). In the present work, we will assume $j_n = 0$ locally at all simulation boundaries. This is expected to impact the solution near the free-space boundaries, as electric current loops that would otherwise cross them are forced to deviate. The effects of this assumption are analyzed in detail in Appendix A, where a validity region, characterized by negligible boundary effects, is clearly identified.

4. Numerical simulations

4.1. Simulation cases and settings

In order to evaluate the effects of the geomagnetic field on a plasma plume expansion, a total of four simulations are presented, which assume charge quasineutrality everywhere, and a plasma plume injected symmetrically at an initial plane $z = 0$ towards $z>0$, and differing only in terms of the magnetic field strength and direction:

- Case 0: null magnetic field (for the purpose of reference).
- Case 1: magnetic field at $\alpha = 0$ deg with the plume axis: $\mathbf{1}_b = [0, 0, 1]$.
- Case 2: magnetic field at $\alpha = 30$ deg with the plume axis: $\mathbf{1}_b = \left[1/2, 0, \sqrt{3}/2\right]$.
- Case 3: magnetic field at $\alpha = 90$ deg with the plume axis: $\mathbf{1}_b = [1, 0, 0]$.

The magnetic field magnitude for Cases 1 to 3 is set to 0.5 Gauss, a typical value for the geomagnetic field at low Earth orbit, and is uniform in magnitude and direction. The rest of the simulation parameters are reported in Table 1 and described hereafter.

The mesh considered by both the electron and PIC models is shown in Fig. 1 at the $y = 0$ cross section. Ion macro-particles are weighted to the nodes of this mesh, while Eq. (11) is discretized with a finite differences scheme of second order. The simulation domain is 2.8 m along x and y, and 30 m along z, featuring a total number of computational nodes of 101×101×301. Parallelepiped cells are considered with a non-uniform size: the mesh spacing is locally minimum close to the boundaries, where larger spatial gradients of the electric current density are expected. This choice permits reducing the numerical truncation errors of the numerical scheme thus increasing the accuracy. More specifically, the axial mesh spacing (i.e. along z) is 2.5 mm close to the injection boundary, reaches a maximum of around 20 cm close to $z = 10$ m, and then diminishes to less than 10 cm at the $z_{max} = 30$ m boundary. Regarding the x and y mesh spacing, this is around 3 cm at the plume core, and diminishes to around 2 cm at the lateral boundaries. In the following sections, results are shown only inside a validity region (1 m × 1 m × 15 m), shown in Fig. 1 by the shaded area, where the imposed boundary conditions have negligible effects, as explained in Appendix A.

The plume injection properties resemble those of the NSTAR ion thruster as in Ref. [23], although its initial non-neutrality in both electric current and density is not modeled here and, for simplicity, only singly-charged Xe ions are considered. These are injected from the

Table 1
Simulation parameters. Charge quasi-neutrality is assumed in the whole domain, and the Hall parameter is limited to 35 by assuming a neutral background density of 2.05 10^{18}m^{-3}. The reference electron density is a consequence of the imposed ion flow and radial profile and refers to the origin $x = y = z = 0$.

Simulation parameters	Units	Values
Initial 95% ion current radius	m	0.14
Injected ions profile	–	Gaussian, axial
Injected Xe ions flow	mg/s	2.38
Injected ions velocity, u_{zi}	km/s	39.1
Injected ions energy	eV	1040
Injected ions initial divergence angle	deg	0.0
Considered collisions for ions	–	None
Reference electron temperature, T_{e0}	eV	1.0
Reference electron density, n_{e0}	m^{-3}	$1.36 \cdot 10^{16}$
Maximum value for the Hall parameter, χ_{max}	–	35
Considered collisions for electrons	–	Elastic with Xe^+ and Xe [23]
Normal electric current density at boundaries, j_n	A/m^2	0.0
PIC time-step	ns	62.5
Total simulation time	ms	3.0
Time-averaging steps for PIC sub-model outputs	–	4000
Time-steps between successive Φ solutions	–	4000
Simulation domain physical dimensions	m	2.8×2.8×30.0
Computational grid points	–	101×101×301

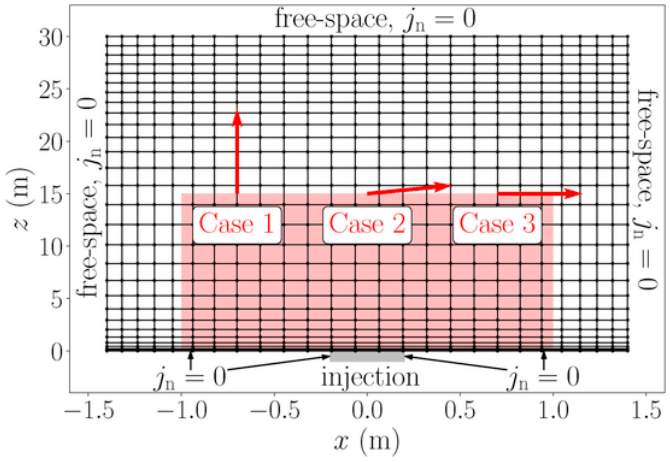

Fig. 1. Sketch of the PIC/fluid mesh cross section at $y = 0$. The yz cross section is analogous to this one. The black lines represent fixed computational coordinates, and, for the sake of clarity, only one every 10 along z and one every 5 along x are shown (therefore, in reality, more nodes are used). The shaded area in red is the validity region, where boundary effects are negligible, while the grey rectangle at $z = 0$ indicates the injection region. The direction of the magnetic field is shown by a red arrow for Cases 1, 2, and 3 (the x and z axis scales are not equal).

$z = 0$ plane from a circular area centered at $x = y = 0$ of radius 20 cm, and with a total mass flow of 24.4 sccm (2.38 mg/s), a purely axial velocity profile corresponding to a mono-energetic beam of 1040 eV, and an initially Gaussian radial profile [8] given by:

$$n_i(r)|_{z=0} = n_{e0} \exp\left[-3\left(\frac{r}{R_0}\right)^2\right] \tag{14}$$

where n_{e0} is the peak quasineutral plasma density at the origin $x = y = z = 0$, $r = \sqrt{x^2 + y^2}$ is the distance from the centerline $x = y = 0$ and R_0 is the 95% ion current radius, assumed to be 0.14 m. The current-free condition in the axial direction ($j_n = 0$) at $z = 0$, is representative of most plasma thrusters, including Hall Effect thrusters, but also ion thrusters operating with a neutralizer, if considered just a few tens of cm downstream from their exit planes.

Since the focus is on electrons, ions are treated as a collisionless species, which are therefore affected only by the electric and magnetic fields. Although a polytropic electron model is also available, as commented in Sec. 3, in this work we have assumed, for simplicity, isothermal electrons, with a reference temperature $T_{e0} = 1$ eV, because electron cooling effects are not expected to affect the physics of interest of this work, which is the plasma plume deviation and compression and the onset and shape of the plasma electric currents. Moreover, electrons collide elastically with both the injected ions and the neutral background [23]. In fact, in order to achieve a good solver convergence with acceptable computational times, while reproducing correctly the physics of the plume expansion (refer to Appendix B for a detailed analysis), the Hall parameter is limited to a certain $\chi_{max} = 35$ by assuming a neutral background density $n_n \simeq 2 \cdot 10^{18}$ m^{-3} (for an electron temperature of 1 eV and Xe atoms).

The simulation features a time-step of $6.25 \cdot 10^{-8}$ s (or 62.5 ns), which is set by the ion crossing time of the smallest PIC cell (at $z = 0$, $\Delta z = 0.25$ cm and ions are injected at roughly 40 km/s axially downstream). The inputs to the electron fluid solver are time-averaged over 4000 steps to reduce PIC noise effects, and, in order to speed up the simulation, this is executed every 4000 time steps to update the Φ corrections, held constant between successive solutions. The simulation physical duration, 3 ms or equivalently 48000 steps, is sufficiently large to reach a stationary solution in terms of the relevant properties (plasma density, electric potential, forces acting on the ions, currents, etc.).

4.2. Reference unmagnetized plasma plume results

In order to assess the effects of the magnetic field on the expanding plasma plume, magnetized plume simulations will be compared with the unmagnetized Case 0, whose results are shown in Fig. 2. Since this plume case is axisymmetric, only $y = 0$ cross sections containing the plume axis are shown.

Subplots 2 (a) and 2 (b) show respectively the electric potential and electron density in the meridian plane $y = 0$. A typical ambipolar potential profile with a mild axial and a steeper radial gradient is observed. The electron density presents a peak slightly above 10^{16} m^{-3} and decreases by approx. 2 orders of magnitude along the plume axis across 15 m. Note that, in this quasineutral unmagnetized simulation, the electric potential is directly related to the electron density through Eqs. (3) and (6).

The electric field intensity and direction resulting from the described potential distribution is shown at $y = 0$ in Fig. 2 (c). The electric field is essentially radially outwards with values between 1 and 30 V/m in most of the plume. The electric field correction due to collisional effects (with both neutrals and ions), which we shall refer to as thermalized electric field, is shown in Fig. 2 (d). In this unmagnetized case, $-\nabla\Phi$ pushes the electrons downstream and balances their momentum loss due to collisions with the neutrals. In fact, referring to Eq. (7), $\boldsymbol{j}_e \times \boldsymbol{B} = 0$ and the collisional term on the right hand side is directed upstream, as it represents an electron momentum loss with a still neutral background (hence $|j_e| > |j_c|$). Nevertheless, this thermalized electric field is at least 2 orders of magnitude smaller than the average electric field (0.05 V/m on average, versus an average electric field of 5 V/m). This means that the neutral background has a negligible effect on the plume expansion in this case (ions, in fact, are injected with an energy of 1040 eV, so they lose around 0.1% of their total energy due to this field).

From the thermalized electric field $-\nabla\Phi$, it is then straightforward to obtain both the electron and electric current densities, shown in Fig. 2 (e) and (f). Regarding the former, it presents a peak value of around 70 A/m^2 at the plume injection plane (where it is identically equal to the ion current density) and is directed predominantly in the axial direction to neutralize the ion current in the whole domain. In this unmagnetized case, the net electric current density is dominated by collisions with the neutrals and, given the lowly collisional character of the plasma, it is expected to be small. In fact, as shown in subplot (f), it is almost 2 orders of magnitude smaller than the ion/electron current density, presents a peak value of about 1.5 A/m^2 slightly downstream from the injection plane, and the meridian electric current loops that appear in this case are small.

4.3. Magnetic field influence on the electric field in the plume

The electron conductivity and the Hall parameter affecting the magnetized electron model solution are shown at the $x = 0$ plane in Fig. 3 (a) and (b) for Case 3 (representative of the other cases as well). The scalar conductivity is maximum at the injection region (with values of up to 500 Ω^{-1}m^{-1}), since it is proportional to the electron density, and the neutral background is uniform. Regarding the Hall parameter, it is minimum close to the injection plane with values around 10, and, as the ion-electron collision frequency decreases with the plume expansion (the electron-neutral collision frequency, on the other hand, is constant due to the assumed uniform neutral background), it tends asymptotically to $\chi_{max} = 35$, both radially outwards and axially downwards.

Figs. 4 and 5 show the thermalized potential and its gradient (i.e. the thermalized electric field, or the net field felt by the electrons due to magnetization and collisional effects) for the three magnetized plume cases, respectively in the $y = 0$ and in the $x = 0$ planes (Cases 1 to 3). Now, contrary to the unmagnetized case, the thermalized poten-

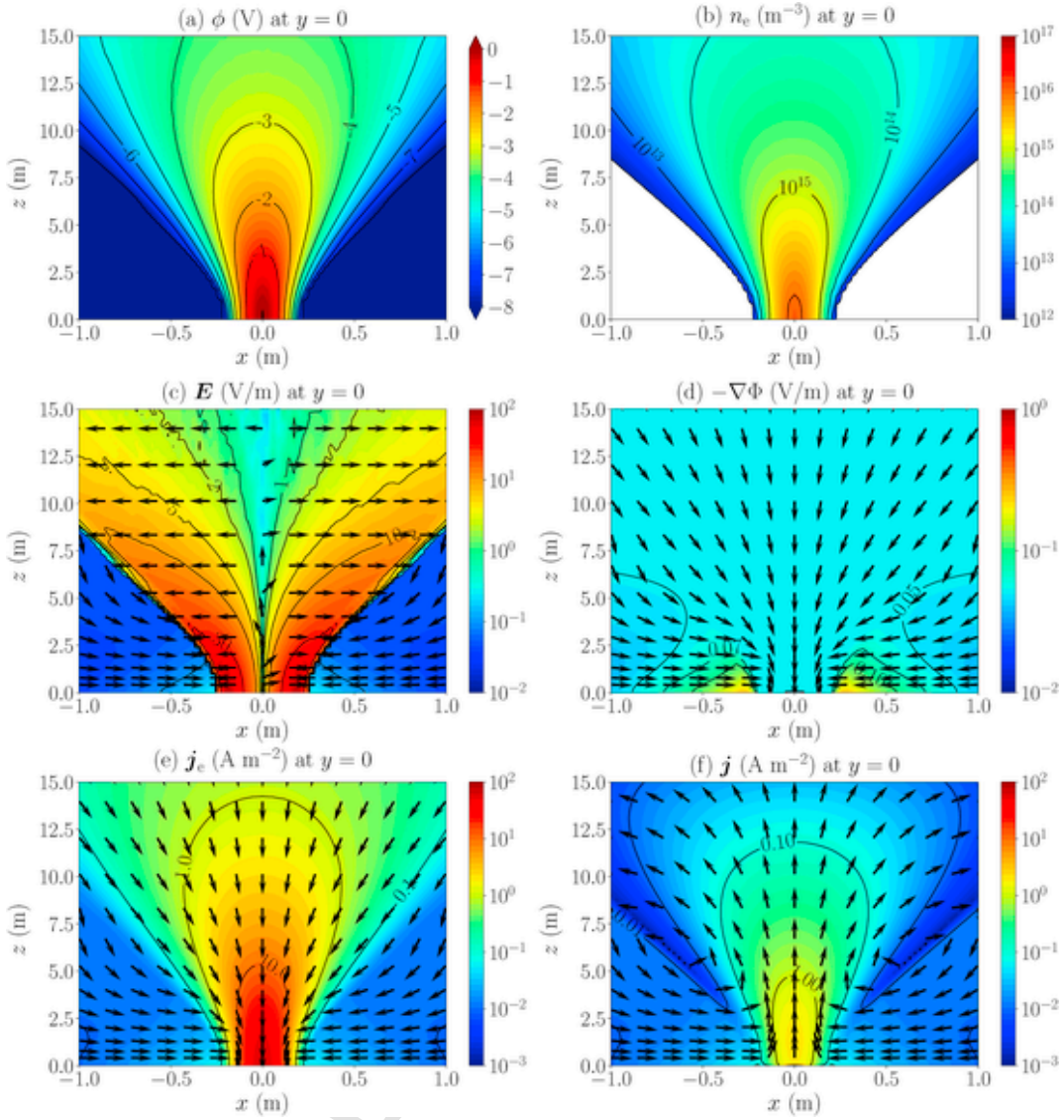

Fig. 2. Case 0 (unmagnetized plume) results at $y = 0$: (a) electric potential, (b) electron density, (c) electric field intensity and direction, (d) thermalized electric field intensity and direction, (e) electron current density and direction (opposite to electron fluid velocity), and (f) electric current density and direction. All properties are symmetric with respect to the plume axis $x = y = 0$, so the $x = 0$ cross sections have been omitted.

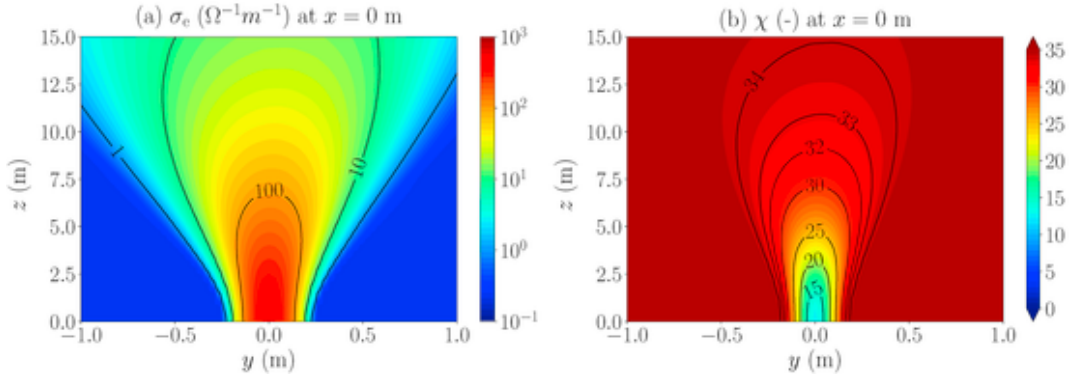

Fig. 3. (a) Electron conductivity and (b) Hall parameter at $x = 0$ for Case 3. Both properties are nearly symmetric with respect to the plume axis $x = y = 0$ and are representative of all magnetized cases (1–3), regardless the field direction, which only produces minor changes.

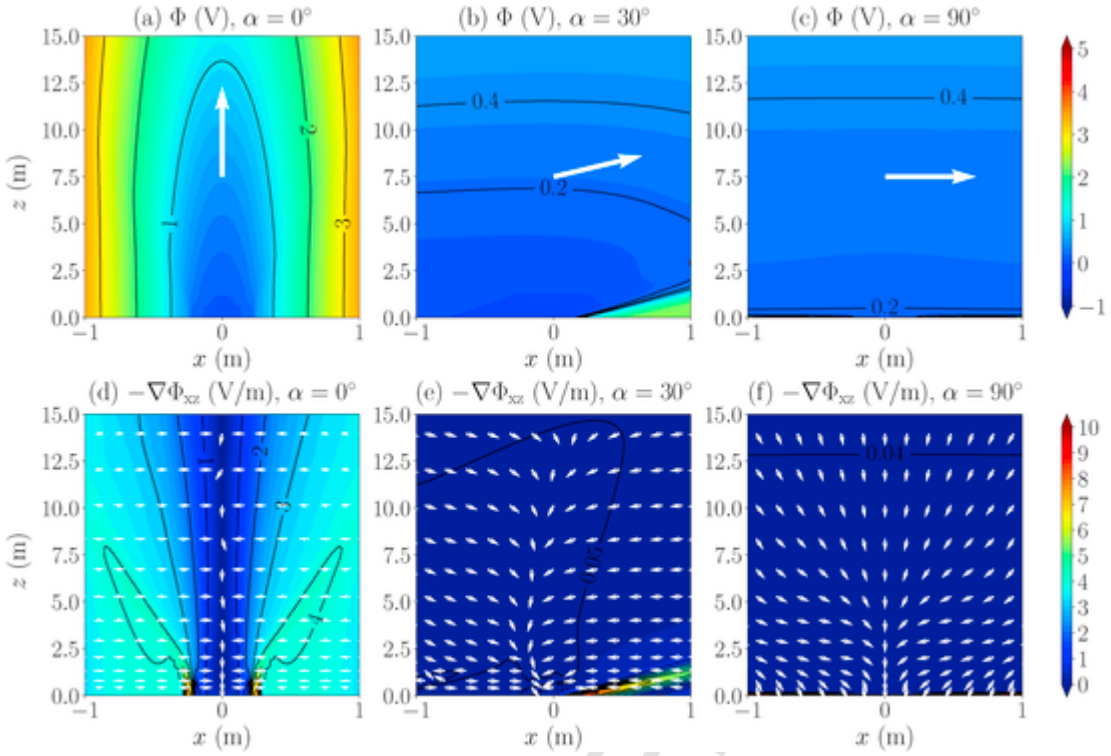

Fig. 4. Thermalized potential Φ and its in-plane gradient $-\nabla\Phi_{xz} = -\left(\partial\Phi/\partial x\,\mathbf{1}_x + \partial\Phi/\partial z\,\mathbf{1}_z\right)$, with magnitude and direction ($\mathbf{1}_x, \mathbf{1}_z$ are the unit vectors along x, z), at $y = 0$, for (a,d) Case 1, (b,e) Case 2, and (c,f) Case 3. The magnetic field is completely contained in the xz plane and its direction is shown by a white big arrow. Notice that the figure has different scales for x and z.

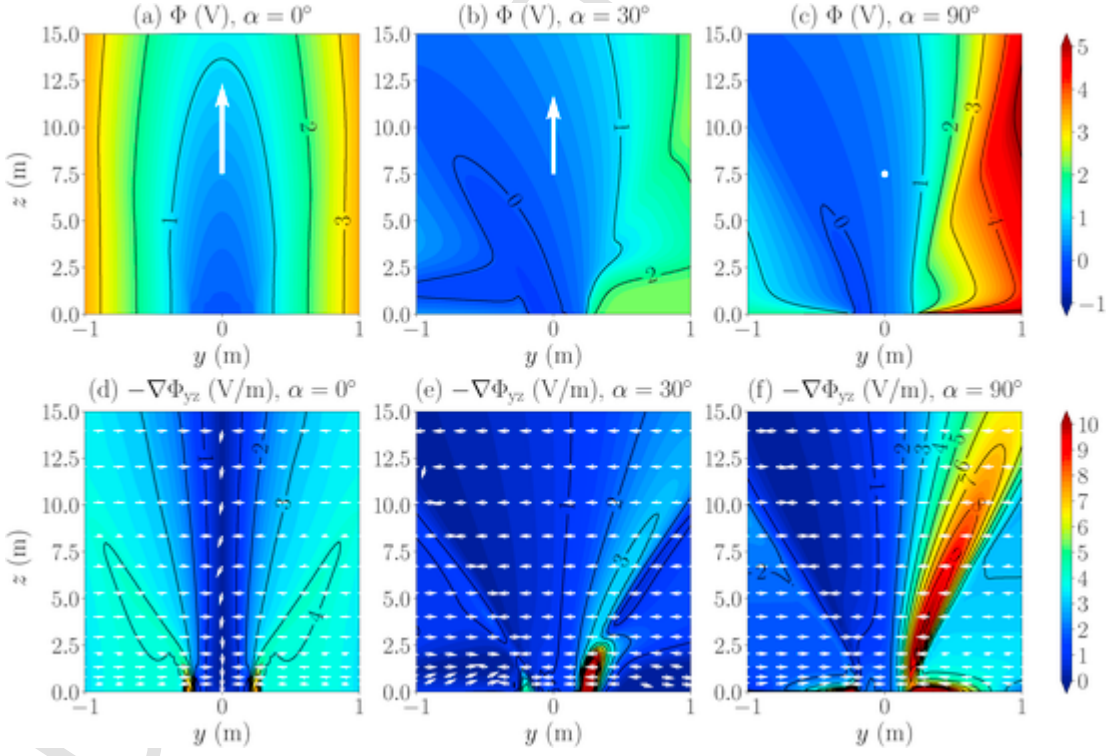

Fig. 5. Thermalized potential Φ and its in-plane gradient $-\nabla\Phi_{yz} = -\left(\partial\Phi/\partial y\,\mathbf{1}_y + \partial\Phi/\partial z\,\mathbf{1}_z\right)$, with magnitude and direction ($\mathbf{1}_y, \mathbf{1}_z$ are the unit vectors along y, z), at $x = 0$, for (a,d) Case 1, (b,e) Case 2, and (c,f) Case 3. The magnetic field projection onto the yz plane is shown by a white big arrow (in subplots (b) and (e) it has an out of plane component, while in subplots (c) and (f), it is directed towards the reader). Notice that the figure has different scales for y and z.

tial is dominated by the magnetic field ($\chi \simeq 35$), and hence the collisional effects only play a minor role.

In Case 1 (axial magnetic field), shown in subplots (a) and (d) of both figures, the solution in terms of Φ is clearly axisymmetric and, as shown in subplots (d), the thermalized electric field is predominantly radial and inward towards the centerline. This produces plume channelling, an effect that reduces the plume divergence and is physically caused by the reduced radial mobility of the magnetized electrons.

In Case 2 ($\alpha = 30$ deg), shown in subplots (b) and (e) of Figs. 4 and 5, the symmetry of the solution is lost. In the $y = 0$ plane (Fig. 4), which contains the magnetic field vector, only collisions play a role, and indeed they produce a mild xz (in-plane) component of the thermalized electric field, which is similar, in magnitude, to the one observed in the unmagnetized case (0.05 V/m, see Fig. 2 (d)). In the $x = 0$ plane (Fig. 5), on the other hand, collisions have a negligible effect, and the thermalized electric field is determined primarily by the Lorentz force on the electrons ($-\nabla\Phi \simeq -\boldsymbol{u}_e \times \boldsymbol{B}$, from Eq. (7)). In a globally current free plume, the integrated Lorentz force on the electrons is equal and opposite to the integrated Lorentz force on the ions, which has a positive y component ($B_x u_{zi} > 0$). Therefore, the thermalized electric field $-\nabla\Phi$ tends to compensate, on average, the $+y$ Lorentz force on the ions. For an axial ion velocity $u_{zi} = 39.1$ km/s, and a magnetic field x-component $B_x = 0.25$ G, the Lorentz force per unit ion charge (or equivalently the induced electric field in the ions reference frame) is $B_x u_{zi} \simeq 1$ V/m. If we look at Fig. 5 (e), we see that, at the centerline, the thermalized electric field is of that order, so that ions nearly advance in straight line. The asymmetry in the thermalized potential gradient induces the compression of the plume along y, as further commented in Sec. 4.4.

A similar phenomenon occurs in Case 3 ($\alpha = 90$ deg, i.e. a magnetic field totally perpendicular to the plume). Now, the x-component of the magnetic field is twice as large (0.5 G), so the thermalized electric field along y is twice as large (2 V/m) as expected and as shown in Fig. 5 (f).

The resultant total electric field, $\boldsymbol{E} = -\nabla h_e/e - \nabla\Phi$, at $x = 0$ and at $z = 10$ m is finally shown in Fig. 6 for the three magnetized simulations.

Comparing the electric field magnitude of Case 1 in Fig. 6 (a) and (d) with that of the unmagnetized plume (Fig. 2 (c)), it is immediately clear that the outward radial electric field is lower in this magnetized field case, due to the reduced mobility of the electrons in the cross-field direction. While in the unmagnetized plume case, the field is always outward at whatever downstream cross section, in Case 1, the radial electric field decreases more quickly downstream and inverts its direction (becoming inward at low radii) at distances above $z = 12 - 13$ m, as it can be appreciated in Fig. 6 (a). This induces a lower divergence increase of the plume and hence a channelling effect of the magnetic field in that direction, which is analyzed in the next section.

The symmetry of the unmagnetized and axial magnetic field cases is completely lost in Cases 2 and 3, shown in Fig. 6 (b), (c), (e) and (f). In Case 2 (subplots (b) and (e)), the asymmetric magnetic field effects are already very patent, and the location of the $E_{xy} = 0$ point gradually moves towards increasing y as the plume expands. As mentioned above, at the plume centerline, the electric field has a negative y component that balances out the Lorentz force on the ions. In Case 3 (subplots (c) and (f)), the asymmetry is even stronger, and the in-plane electric field at $z = 10$ m presents a null point at around 0.5 m from the plume centerline.

Finally, it is interesting to notice that, in the lateral regions of the plasma plume, the electric field is always inward in all magnetized plume cases (see Fig.6 (a)–(c)). This is due to the fact that the mobility of the electrons in the y direction is strongly reduced in all cases, being $\boldsymbol{B}$ contained in the xz plane.

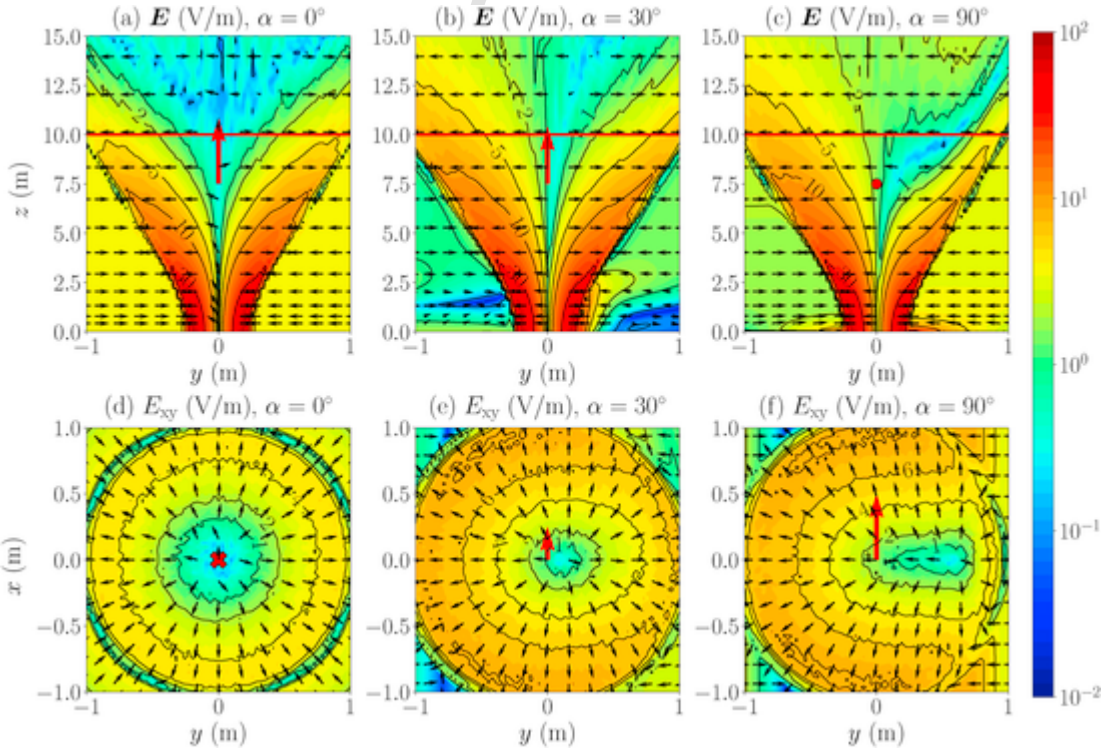

Fig. 6. Electric field magnitude and in-plane direction for (a,d) Case 1, (b,e) Case 2, and (c,f) Case 3. The $x = 0$ cross section is shown in subplots (a), (b) and (c), while the $z = 10$ m cross section is shown in subplots (d), (e) and (f). This latter cross section is indicated in subplots (a), (b) and (c) by a red solid line. The magnetic field projection onto the shown planes is indicated by a thick red arrow in all subplots (in subplot (c), the field is directed towards the reader, while in subplot (d) it is toward the page). (For interpretation of the references to colour in this figure legend, the reader is referred to the Web version of this article.)

4.4. Plasma plume deformation due to the magnetic field

In the previous section we have found that, at the centerline, the thermalized field $-\nabla\Phi$ nearly compensates the Lorentz force on the ions. In fact, the stationary momentum balance equation for cold ions (i.e. with negligible temperature) is

$$\nabla\cdot\left(m_i n_e \boldsymbol{u}_i\boldsymbol{u}_i\right) = e n_e\left(\boldsymbol{E}+\boldsymbol{u}_i\times\boldsymbol{B}\right), \tag{15}$$

where we have assumed quasineutrality $n_e = n_i$ and neglected collisional effects on the ions. Solving for $\boldsymbol{E}$ in Eq. (2), and substituting into Eq. (15), this takes the form:

$$\nabla\cdot\left(m_i n_e \boldsymbol{u}_i\boldsymbol{u}_i\right) = -\nabla p_e + \boldsymbol{j}\times\boldsymbol{B} + \frac{m_e\nu_e}{e}\left[\boldsymbol{j}+\boldsymbol{j}_c-\boldsymbol{j}_i\right]. \tag{16}$$

The ion acceleration has three different contributions: *(i)* a purely electron-thermal one, which is independent of magnetization and is caused by the scalar electron pressure gradient ($-\nabla p_e$), *(ii)* a magnetic one $\boldsymbol{j}\times\boldsymbol{B}$, which is strictly related to the existence of a net electric current, and *(iii)* a collisional one that is small for quasi-collisionless plasmas ($\nu_e \to 0$).

In an unmagnetized plume, $\boldsymbol{j}\times\boldsymbol{B}$ is zero, and the ion acceleration term is balanced out by the electron pressure gradient term alone (collisions have a negligible effect on the ion momentum, although they dictate the electron currents in this case). In our magnetized plume cases, on the other hand, local electric currents can exist and the ion inertial acceleration is balanced out by the sum of both pressure gradient and magnetic $\boldsymbol{j}\times\boldsymbol{B}$ terms. If the plume is globally current-free, however (see Sec. 3.1), and the external magnetic field is uniform, the integral of the $\boldsymbol{j}\times\boldsymbol{B}$ force in the domain must vanish, as shown in Ref. [8].

As a consequence, the magnetic force cannot produce a net deflection of the plume momentum, although it can clearly deform it in non-trivial ways since $\boldsymbol{j}\times\boldsymbol{B}$ is non-zero locally. Fig. 7 (a) to (c) show the relative change (with respect to Case 0) of the plasma density at $z = 10$ m for the 3 magnetized plume cases. In Case 1 ($\alpha = 0$), the relative plasma density increases up to 15% at the centerline, while at higher radii, the channelling effect produces a relative density reduction. In Case 2 ($\alpha = 30$ deg), on the other hand, the deformation is clearly asymmetric and a non-negligible compression along the y direction can be observed. Finally, in Case 3 ($\alpha = 90$ deg), the compression is clearly along y and the relative density change reaches positive peaks around $+10\%$, and negative peaks below -30%. This non-symmetric density change is an effect of the Lorentz force on the ions, which, in this case, is always directed towards $+y$. Qualitatively, the described plume deformation is in good agreement with the findings by Korsun et al. [5,6], who also observed plume compression along y in the perpendicular field Case 3 and plume channeling in Case 1, although they did not study any intermediate angle case (like Case 2).

The total force balance commented above can also be explained by the onset of a balancing electric field, if we consider the individual electron trajectories in the collisionless limit ($\chi \to \infty$). In fact, in the $\alpha = 90$ deg case, electrons cannot traverse the magnetic field lines and neutralize the ion current with $\boldsymbol{u}_e \simeq \boldsymbol{u}_i$ (on average, not locally), unless an $\boldsymbol{E}\times\boldsymbol{B}$ field makes their gyrocenter drift in the z direction, with the same velocity as the ion velocity. The required electric field to produce such an average drift is $-\boldsymbol{u}_i\times\boldsymbol{B}$, so that $-\left(\boldsymbol{u}_i\times\boldsymbol{B}\right)\times\boldsymbol{B}$ is along $+z$. The limited mobility of electrons along z at first produces a drift along y due to an axial electric field (arising from the fact that electrons are left behind with respect to ions). This drift only affects electrons (ions are not magnetized) so that the infinitesimal charge separation along y produces the ambipolar E_y field that is responsible of the requested mean axial drift.

In order to verify numerically the absence of a net plasma plume deflection, the total electric and magnetic force acting on the ion macro-particles has been computed as:

$$\begin{aligned}\boldsymbol{F} &= \sum_p eW_p\left(\boldsymbol{E}\left(\boldsymbol{r}_p\right)+\boldsymbol{u}_p\times\boldsymbol{B}\left(\boldsymbol{r}_p\right)\right)\\ &= \iiint e n_e\left(\boldsymbol{E}+\boldsymbol{u}_i\times\boldsymbol{B}\right)\mathrm{d}V,\end{aligned} \tag{17}$$

where p is the macro-particle index, and the summation extends to all macro-particles that are located within the validity region volume ($z \in [0, 15]$ m), with differential volume $\mathrm{d}V$. The evolution of the y component of this force F_y (along the dominant Lorentz force direction), and of its electric and magnetic components, is shown in Fig. 8 (a) for Cases 2 and 3. In all numerical simulations, for t<1 ms, an artificial Boltzmann equilibrium $e\varphi = T_{e0}\ln\left(n_e/n_{e0}\right)$ is assumed in the whole domain, in order to highlight the importance of including magnetization effects in the model. In fact, this Boltzmann electric field is not capable of balancing out the magnetic force and a net force along y is observed. As soon as the magnetized plume model is activated (first vertical dashed arrow, at $t = 1$ ms), the magnetic force (Lorentz) starts to be balanced out by the electric field force, in both Cases 2 and 3. As a consequence, also the y deviation of the center of mass (COM) of the plume ions abruptly changes from around 3.5 cm to zero, as shown in Fig. 8 (b).

Finally, Fig. 8 (c) shows the xy position of the plasma plume COM at $z = 10$ m, at $t = 1$ ms (i.e. before the activation of the magnetized electron model) and at the end of the simulation ($t = 3$ ms). A rude estimate for the initial y displacement due to the Lorentz force can be obtained by considering a uniform acceleration of ions with a constant axial velocity, that is $\Delta y = \left(eu_{zi}B_x/m_i\right)\left(\Delta z/u_{zi}\right)^2/2$. For the considered ion velocity (39.1 km/s), magnetic field x-component (0.25 and 0.5 G for respectively Cases 2 and 3), and given $\Delta z = 10$ m and $m_i = 2.18\cdot 10^{-25}$ kg (xenon ions), this displacement amounts to 2.3 cm and 4.7 cm

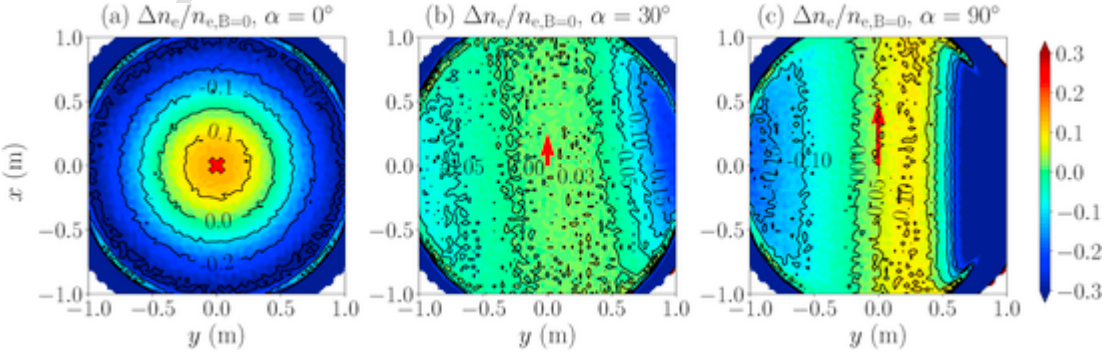

Fig. 7. Plasma density relative variation with respect to the unmagnetized plume case, at $z = 10$ m for (a) Case 1, (b) Case 2, and (c) Case 3. The magnetic field projection onto the shown plane is indicated by a thick red arrow in all subplots (in subplot (a), the field is toward the page). (For interpretation of the references to colour in this figure legend, the reader is referred to the Web version of this article.)

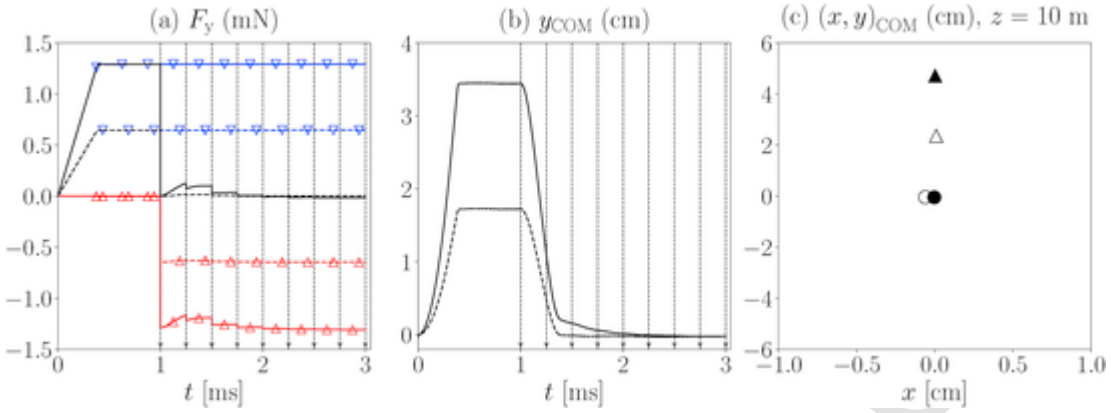

Fig. 8. Time evolution in Case 2 (dashed lines) and Case 3 (solid lines) of (a) electric force (red lines, upwards triangles), magnetic force (blue lines, downwards triangles) and total force (black lines, no marker) on the plume ions and (b) y position of plasma plume center of mass. Only ions within the validity region $z \in [0, 15]$ m are considered for the computation of both the total forces and the plume center of mass. The vertical dotted lines correspond to the time instants in which a new solution for Φ is computed. (c) Center of mass position of the plume cross section at $z = 10$ m, at $t = 1$ ms (triangles) and at $t = 3$ ms (circles), for Case 2 (empty markers) and Case 3 (filled markers). Notice that the x and y scales are different. (For interpretation of the references to colour in this figure legend, the reader is referred to the Web version of this article.)

for respectively Cases 2 and 3, which is consistent with the deviations shown in Fig. 8 (c) before activating the magnetized electron solver (triangles). At the end of the simulation, in both cases, the center of mass is perfectly aligned with the plume centerline $x = y = 0$ (apart from negligible numerical errors).

4.5. Induced electron and electric currents

Once Φ is computed, it is straightforward to obtain both the electron current density $\boldsymbol{j}_e$ from Eq. (8) and hence the total electric current density $\boldsymbol{j}$, by summing the known ion current density $\boldsymbol{j}_i$ (from the PIC model). While in the unmagnetized case, shown in Fig. 2 (e) and (f), no significant electric current loops formed and electron streamlines closely resembled those of the ions (to neutralize their current), in the magnetized cases, things change substantially. The electron streamlines from $\boldsymbol{u}_e = -\boldsymbol{j}_e / (en_e)$ are shown in Fig. 9 (a) to (c) for Cases 1 to 3.

In the axial magnetic field Case 1 (subplot (a)), the electron streamlines are essentially helicoidal. This shape originates from the combination of the bulk axial electron motion which is necessary to neutralize the ion current (the plasma plume is forced to be current free, along z

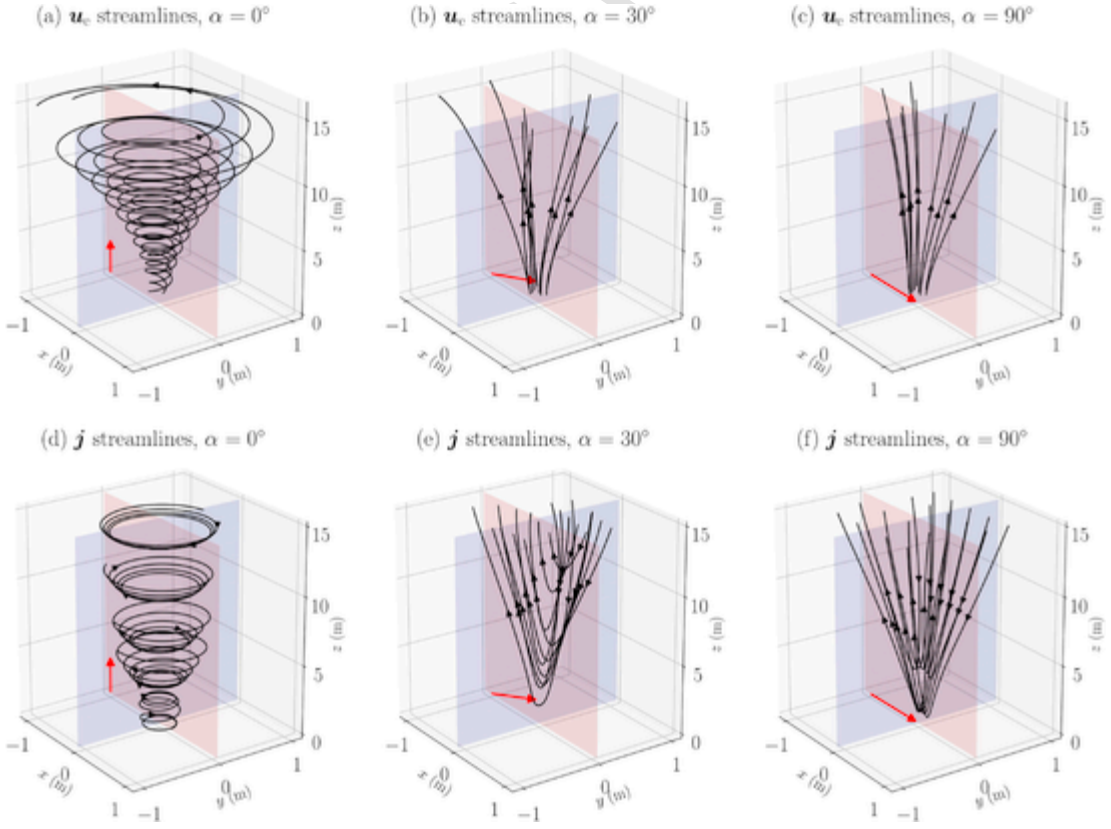

Fig. 9. (a,b,c): three-dimensional electron streamlines (from $\boldsymbol{u}_e$) for (a) Case 1, (b) Case 2, and (c) Case 3. (d,e,f): three dimensional electric current streamlines (from $\boldsymbol{j}$) for (d) Case 1, (e) Case 2, and (f) Case 3. The magnetic field direction in each case is shown by a red arrow, while the plasma plume is injected from the $z = 0$ plane. The $y = 0$ and $x = 0$ planes are also shown for the sake of clarity (respectively in light red and blue). (For interpretation of the references to colour in this figure legend, the reader is referred to the Web version of this article.)

, at both the $z = 0$ and $z_{max} = 30$ m boundaries), and the induced azimuthal drift due to both the diamagnetic and the $\boldsymbol{E} \times \boldsymbol{B}$ drifts (which are anti-parallel), or equivalently the net drift due to $\nabla\Phi$ (which includes both drifts). In Cases 2 and 3 (subplots (b) and (c)), on the other hand, the helicoidal motion is disrupted and almost disappears, although some electron streamline twisting can still be observed in both cases.

The three-dimensional electric current streamlines are shown in Fig. 9 (d), (e) and (f) for the 3 magnetized cases. In Case 1 (subplot (d)), the dominating electric currents are obviously azimuthal, while in the oblique field cases (subplots (e) and (f)), the electric current loops have an important axial component. For the chosen boundary conditions, the artificial closure of the electric current loops occurs at the z_{max} boundary of the simulation box, not shown here, since it is located at $z = 30$ m and is outside of the defined validity region.

Fig. 10 (a), (b) and (c) show the electric current density magnitude and its direction at $x = 0$, Fig. 10 (d), (e) and (f) show the axial electric current density at $z = 10$ m, and Fig. 10 (g), (h) and (i) show the in-plane electric current density at $z = 10$ m. As already mentioned, in Case 1 (subplots (a), (d) and (g)), the electric current density is predominantly azimuthal, except close to the plume centerline, where it is axially oriented (no azimuthal currents can exist there). Nevertheless, a dim axial electric current loop exists also in Case 1, consisting in a negative current density (down to -1 A/m^2 at $z = 10$ m) at the centerline and a positive current density (up to $+0.12$ A/m^2 at $z = 10$ m) in the surrounding regions (refer to Fig. 10 (d)). The azimuthal current density, on the other hand, reaches values as high as 2 A/m^2 at $z = 10$ m.

In Cases 2 and 3, on the other hand, the electric current density is predominantly axial, as shown in subplots (b) and (c), and two counter-moving tubes of electric current appear. This is clear in Fig. 10 (e) and (f), showing the axial electric current density at $z = 10$ m: in Case 2, the axial electric current density is as high as ± 0.8 A/m^2 at $z = 10$ m, while in Case 3, it reaches peak values of around ± 1.5 A/m^2. The in-plane current density for Cases 2 and 3 is no more azimuthal as clearly shown in Fig. 10 (h) and (i) and is negligible compared to the axial current density (more than one order of magnitude lower).

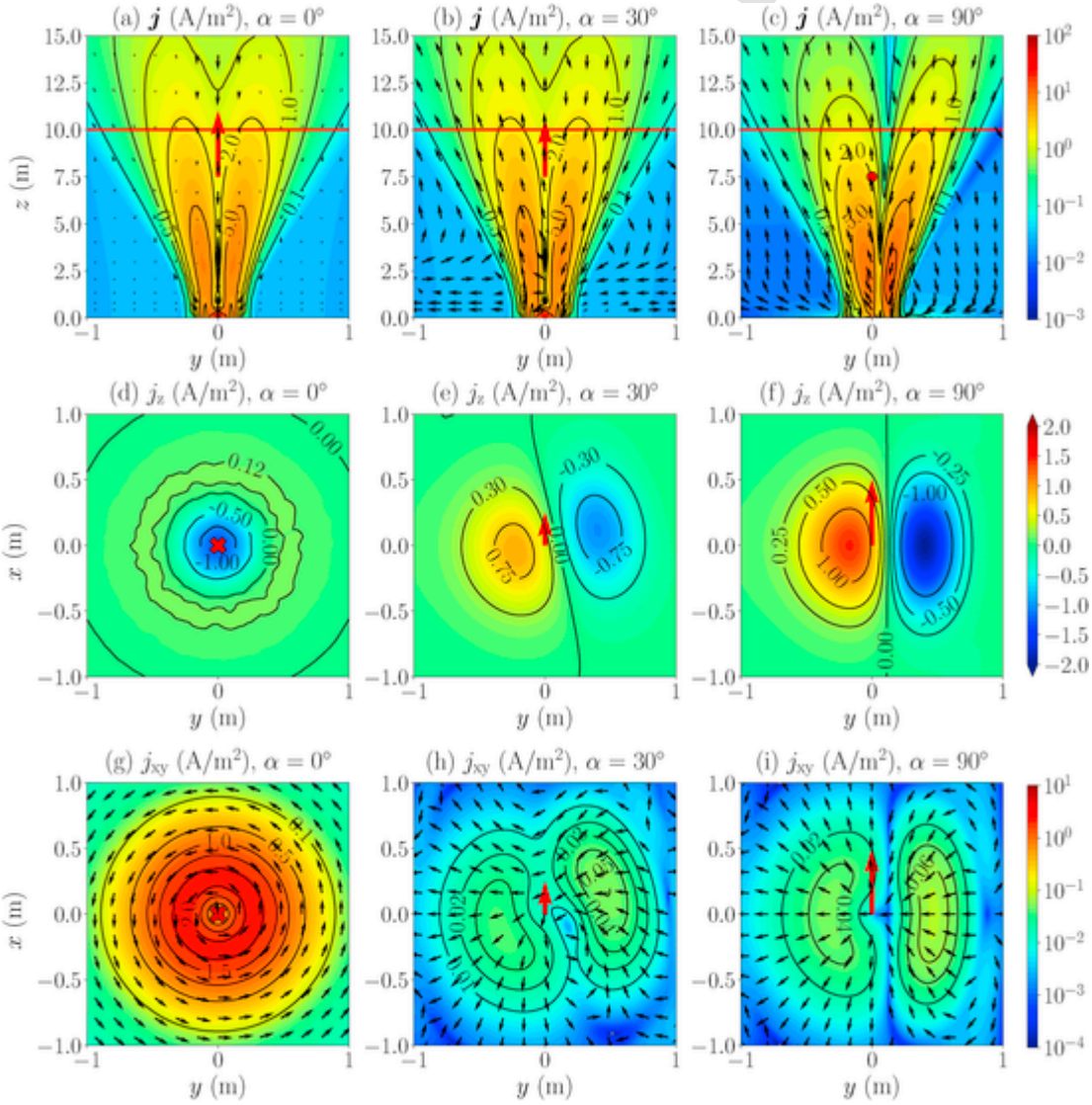

Fig. 10. (a)–(c): electric current density magnitude and in-plane direction at $x = 0$ for (a) Case 1, (b) Case 2, and (c) Case 3. The length of the arrows is proportional to the ratio between the in-plane component and the total intensity. (d) to (f): axial electric current density j_z in the ^{xy} plane at $z = 10$ m, for (d) Case 1, (e) Case 2, and (f) Case 3. (g) to (i): in-plane ^{xy} electric current density at $z = 10$ m, with in-plane direction, for (g) Case 1, (h) Case 2, and (i) Case 3. The $z = 10$ m cross section shown in subplots (d) to (i) is also indicated in subplots (a), (b) and (c) by a red solid line. The magnetic field projection onto the shown planes is indicated by a thick red arrow in all subplots (in subplots (d) and (g), the field is toward the page, while in subplot (c), it is toward the reader). (For interpretation of the references to colour in this figure legend, the reader is referred to the Web version of this article.)

4.6. Diamagnetic plasma response and self-induced magnetic field

Referring to both Figs. 9 and 10, it is interesting to notice the diamagnetic character of the electric current loops.

In the axial Case 1, we have two counteracting electron drifts in the azimuthal direction. Taking the positive drift direction to be clock-wise from the $+z$ axis, we have *(i)* the positive (clock-wise) E_r/B_z drift (where E_r is the radial component of the electric field), and *(ii)* the negative (counter clock-wise) diamagnetic drift $\left(\partial p_e/\partial r\right) / \left(en_e B_z\right)$.

The algebraic sum of these two drifts is given simply by $-\left(\partial\Phi/\partial r\right)/B_z$. Looking at Fig. 5 (a), we can see that $\partial\Phi/\partial r>0$, so electrons drift negatively (counter clock-wise), as shown in Fig. 9 (a), so that the induced magnetic field they would create is in the $-z$ direction, thus opposing to the external one. An order of magnitude for this net drift can be obtained by looking at Fig. 5 (d): at $z = 10$ m, an average radial gradient of 2 V/m is observed, yielding a net counter clock-wise drift of 40 km/s. The $\boldsymbol{E}\times\boldsymbol{B}$ drift, on the other hand, can be estimated at $z = 10$ m from Fig. 6 (d), showing an average radial electric field of 3 V/m, corresponding to a clock-wise drift velocity of 60 km/s. Therefore the diamagnetic drift accounts for around 100 km/s, and the net drift is comparable to each of the two primary contributions.

In the oblique field cases 2 and 3, Fig. 10 (b) and (c) clearly show electric current loops that induce a magnetic field directed into the page, whereas the applied magnetic field is directed out of the page. Therefore, independently of the magnetic field direction, the plasma response is always diamagnetic.

Due to this diamagnetic behavior, we can reasonably assert that the total magnetic field inside the plume will be somewhat smaller than the applied one. The exact computation of the self-induced field requires to solve Ampère's equation $\nabla\times\boldsymbol{B} = \mu_0\boldsymbol{j}$, where μ_0 is the magnetic permeability of vacuum, and is left to future work. Here we simply estimate it roughly with an order of magnitude analysis as $B_{\text{ind}} \approx L\mu_0 j$, where L is a characteristic size of the plasma plume. Assuming a current density of 10 A/m^2, and a characteristic plume diameter of 0.5 m, then the induced magnetic field turns out to be in the order of 0.1 Gauss. This magnitude is smaller but non-negligible with respect to the external geomagnetic field (0.5 Gauss), so the induced magnetic field might play some role, especially near the denser axis of the plume.

5. Conclusions

This paper has presented the three-dimensional analysis of the far-region expansion of a plasma thruster plume into a region with a uniform geomagnetic field. This study has been carried out with a hybrid particle-in-cell/fluid code, featuring particle ions and fluid electrons, which are affected by both an externally applied magnetic field and collisions with the heavy species (ions and neutrals). Using a tensor conductivity formulation, the electron model solves directly for the correction to the collisionless and unmagnetized plasma plume solution, in the form of a thermalized potential gradient, which is determined by both effects.

A set of three simulations has been presented with a uniform geomagnetic field at different angles, which are characteristic of various states of thruster operation at low Earth orbit altitudes. The external magnetic field effects have been identified in terms of electric field, plasma density changes, and generally three-dimensional electric currents.

Regarding the expansion physics, an axial magnetic field focuses the plasma plume, by reducing its divergence angle, and relatedly, it generates azimuthal electric currents. When the magnetic field is at an angle with the plume axis, on the other hand, more complex electric current loops form, with a dominating axial character. The resulting ambipolar electric field allows the electrons to drift with the ions in the axial direction and balances out the integrated effect of the Lorentz force on the plume ions. The non-negligible axial electric currents that develop in the plasma, on the other hand, have the effect of compressing the plume cross section in the direction perpendicular to both the plume axis and the magnetic field. Still, no net momentum deflection of the ion plume is observed, in agreement with the zero integral momentum exchange between a plasma plume in a uniform magnetic field, with no integrated electric currents allowed to flow to infinity [8]. Finally, in all simulated cases, the induced electric current loops are diamagnetic and thus their induced magnetic field tends to oppose the applied field inside the plasma.

Future work shall focus on the following topics: *(i)* combined simulations of both the near and far-region of the magnetized plume, considering the effects of charge-exchange collisions, non-current-free plume injection and charge non-neutrality *(ii)* simulations with some electron cooling (e.g. a polytropic law or a kinetic electron sub-model), and with a more realistic neutral background density, *(iii)* the study of the induced magnetic field effects, by computing a correction to the uniform background field either iteratively, as in Ref. [29], or by solving Ampère's law, *(iv)* the assessment of numerical diffusion effects due to the misalignment between the magnetic field direction and the considered non-uniform rectangular mesh, and *(v)* plume simulations featuring non-uniform and larger magnetic fields, like that of a magnetic nozzle [30].

Acknowledgments

The primary funder of this research was the Comunidad de Madrid (Spain), under PROMETEO-CM project, with grant number Y2018/NMT-4750. Initial support was provided by the Ministerio de Economía y Competitividad (Spain), under project ESP2016-75887-P.

Appendix A. Effects of the boundary conditions

As commented in Sec. 3.1, a locally-zero normal electric current j_n is assumed at the boundaries to solve numerically Eq. (11) for the thermalized potential. Nevertheless, the effects of this assumption have to be clearly identified with an accurate study. In this Appendix, they have been evaluated by comparing simulations with three different domain extensions for each of the three magnetic field directions ($\alpha = 0, 30, 90$ deg):

- Small domain size: 2.4 m × 2.4 m × 20 m
- Intermediate domain size: 2.6 m × 2.6 m × 25 m
- Large domain size: 2.8 m × 2.8 m × 30 m

The results are shown in Fig. 11 Fig. 11 (a)–(f), for the electric current density.

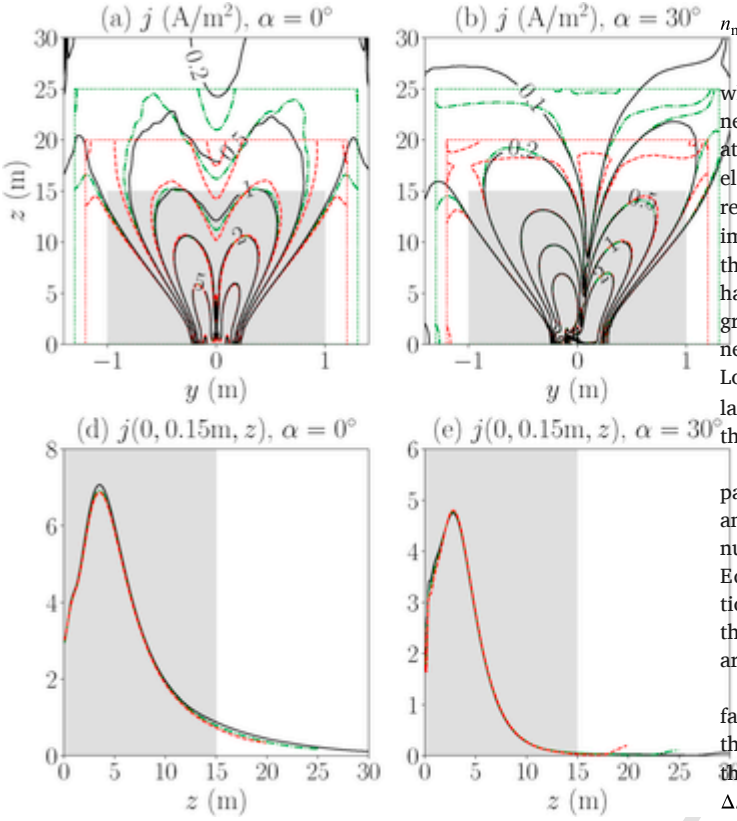

Fig. 11. (a,b,c) magnitude of the electric current density at $x = 0$, and (d,e,f) its evolution along z. Subplots (a) and (d) refer to Case 1, (b) and (e) refer to Case 2, and (c) and (f) refer to Case 3. Results for the large domain size are shown by black solid lines, the intermediate domain size is shown with green dash-dot lines, and the small domain size is shown by red dashed lines. The shaded area indicates the validity region, where boundary effects are negligible.

Case 3 ($\alpha = 90$ deg) appears to be the most affected by the boundary conditions. This is not surprising as the natural electric current loops are essentially axial in this case, so that the imposition of a zero normal current at the downstream boundary forces the electric current loops to close there. Nevertheless, from Fig. 11 (c), the obtained solutions with 25 and 30 m axial domain size are essentially the same in a region defined by $(x, y) \in [-1, 1]$ m and $z \in [0, 15]$ m. This is even clearer by observing the evolution of the current density along the direction $y = 0.15$ m, shown in Fig. 11 (f). The observed convergence obtained by extending the domain size from 20 to 25 m, allows to define the above cited region (shown by a shaded rectangle in the figure) as an effective validity region.

For Cases 1 and 2 (with respectively $\alpha = 0$ and 30 deg), the effects of the boundaries are very local and the validity region would be larger than in Case 3. This is also expected since the electric current loops have a negligible (smaller) axial component in Case 1 (2), when compared to Case 3. Nevertheless, for uniformity, the analysis domain of Sec. 4 is restricted to this validity region, and the large simulation domain results are considered, being the most accurate ones in terms of boundary effects.

Appendix B. Effects of the neutral background

As mentioned in Sec. 4.1, a still and uniform background of neutrals is considered to limit the Hall parameter downstream to $\chi_{\max} = 35$. This neutral density is computed as:

$$n_n = \frac{eB}{\chi_{\max} m_e R_{en}(T_e)}, \tag{18}$$

where R_{en} is the electron collisional momentum transfer rate to the neutrals, which, for the assumed electron temperature (1 eV) and Xe atoms, takes the value of $1.23 \cdot 10^{-13}$ m^3/s [23]. Moreover, a minimum electron conductivity $\sigma_{e,\min} = 0.25\Omega^{-1}m^{-1}$ is also assumed for the correct convergence of Eq. (11), which is equivalent to considering a minimum plasma density $n_{e,\min} = \sigma_{e,\min} B/(e\chi_{\max}) = 2.2 \cdot 10^{12}$ m^{-3}. While these limitations on the minimum electron conductivity and density have negligible physical effects, the assumed uniform neutral background can have a huge impact on the electron dynamics and its effects need to be assessed. In fact, a realistic neutral background density at Low Earth orbit altitudes (400–800 km) can vary, depending on the solar activity, between 10^{12} and 10^{15} m^{-3} [31], which is much smaller than the assumed neutral background density ($2 \cdot 10^{18}$ m^{-3}).

If a realistic neutral background density were considered, the Hall parameter would be quickly determined by the electron-ion collisions and become larger than 1000 farther downstream, thus yielding to large numerical truncation errors of the finite differences scheme used to solve Eq. (11). This problem can be solved by using a finer mesh (the truncation error decreases with the square of the cell size), especially close to the boundaries, or by limiting the maximum value of the Hall parameter artificially. Both approaches are used here.

The first solution presents increasing computational time costs. In fact, increasing the resolution close to the boundaries while maintaining the total number of mesh nodes, reduces the maximum PIC time step that fulfills the Courant-Friedrichs-Levy (CFL) condition: $v\Delta t < \Delta l$, where Δl is the smallest mesh element size and v is the maximum ion velocity. So, the computational time scales with the inverse of the smallest mesh element size.

In this Appendix, the effects of this background on the obtained solution are evaluated. A set of simulations with a varying neutral density to reproduce a maximum Hall parameter of 10, 20, 30, 35 (nominal), 40, 50 and 100, has been carried for Case 3 ($\alpha = 90$ deg), although a similar behavior is expected for Cases 1 and 2. The integrated positive electric current (i.e. moving through the positive electric current tube, featuring $j_z > 0$) at the $z = 10$ m cross section is computed for each of these $\chi_{\max}$ cases and plotted in Fig. 12Fig. 12 (a).

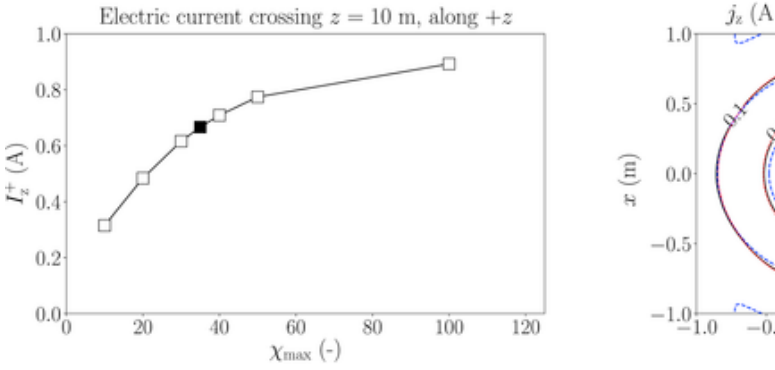

Fig. 12. (a) Integrated current flowing through the positive electric current tube ($j_z > 0$) at $z = 10$ m as a function of the maximum Hall parameter. (b) Comparison of the axial electric current density at $z = 10$ m for $\chi_{\max} = 20$ (blue dashed line), $\chi_{\max} = 35$ (black solid line), and $\chi_{\max} = 50$ (red dotted line). Case 3 ($\alpha = 90$ deg) is considered here.

The integrated current tends to saturate with the Hall parameter, although, at the considered $\chi_{\max} = 35$ case (filled square), such saturation has not been achieved yet. Observing Fig. 12 (b), however, we can appreciate a certain convergence of the solution, since the electric current contour lines corresponding to $\chi_{\max} = 35$ are closer to the ones ob-

tained for $\chi_{max} = 50$ than for $\chi_{max} = 20$. The effect of increasing the maximum Hall parameter (or equivalently decreasing the neutral background density) is therefore to make the integrated and peak electric current density in the counter-moving current tubes higher. This yields to a higher local deformation force $f_y = j_z B_x$ acting on the plume ions (refer to Eq. (16)), although the total integrated force along *y* is always zero. In fact, B_x is constant and, for continuity, the integrated current in the positive current tube ($j_z>0$) is equal and opposite to the one flowing through the negative current tube ($j_z<0$). This means that the global force balance commented in Sec. 4.4 is achieved regardless of the maximum allowed Hall parameter. Nevertheless, a larger plume deformation is expected, although with the same qualitative character.

References

[1] I G Mikellides, G A Jongeward, I Katz, D H Manzella, Plume modeling of stationary plasma thrusters and interactions with the express-A spacecraft, J. Spacecraft Rockets 39 (No. 6) (Nov. 2002) 894–903.

[2] C Bombardelli, J Peláez, Ion beam shepherd for contactless space debris removal, J. Guid. Contr. Dynam. 34 (No. 3) (May 2011) 916–920.

[3] M Merino, E Ahedo, C Bombardelli, H Urrutxua, J Peláez, Ion beam shepherd satellite for space debris removal, in: L T DeLuca, C Bonnal, O J Haidn, S M Frolov, Progress in Propulsion Physics, IV, EDP Sciences, Les Ulis, France, 2013, pp. 789–802 of EUCASS Advances in Aerospace Scienceschap. 8.

[4] F Cichocki, M Merino, E Ahedo, Spacecraft-plasma-debris interaction in an ion beam shepherd mission, Acta Astronaut. 146 (2018) 216–227.

[5] A Korsun, E Tverdokhlebova, "Geomagnetic Field Perturbation by a Plasma Plume," *25th International Electric Propulsion Conference*, Electric Rocket Propulsion Society, Fairview Park, OH, Fairview Park, OH, 1997.

[6] A Korsun, E Tverdokhlebova, F Gabdullin, Mathematical model of hypersonic plasma flows expanding in vacuum, Comput. Phys. Commun. 164 (No. 1–3) (2004) 434–441.

[7] M Wartelski, C Theroude, C Ardura, E Gengembre, "Self-Consistent Simulations of Interactions between Spacecraft and Plumes of Electric Thrusters," 33rd International Electric Propulsion Conference, Electric Rocket Propulsion Society, Fairview Park, OH, Washington D.C., October 7-10, 2013 paper 2013-73.

[8] M Merino, F Cichocki, E Ahedo, Collisionless Plasma thruster plume expansion model, Plasma Sources Sci. Technol. 24 (No. 3) (2015) 035006.

[9] A Ortega, I Katz, I Mikellides, D Goebel, Self-consistent model of a high-power Hall thruster plume, IEEE Trans. Plasma Sci. 43 (No. 9) (2015) 2875–2886.

[10] I Mikellides, I Katz, Numerical simulations of Hall-effect plasma accelerators on a magnetic-field-aligned mesh, Phys. Rev. 86 (No. 4) (2012) 046703.

[11] D Tskhakaya, K Matyash, R Schneider, F Taccogna, The particle-in-cell method, Contrib. Plasma Phys. 47 (No. 8–9) (2007) 563–594.

[12] F Taccogna, R Schneider, S Longo, M Capitelli, "Kinetic simulations of a plasma thruster, Plasma Sources Sci. Technol. 17 (No. 2) (2008) 024003.

[13] H Wang, W Jiang, Y Wang, Implicit and electrostatic particle-in-cell/Monte Carlo model in two-dimensional and axisymmetric geometry: I. Analysis of numerical techniques, Plasma Sources Sci. Technol. 19 (No. 4) (2010) 045023.

[14] J Wang, D Han, Y Hu, Kinetic simulations of plasma plume potential in a vacuum chamber, IEEE Trans. Plasma Sci. 43 (No. 9) (2015) 3047–3053.

[15] G Lapenta, Automatic adaptive multi-dimensional particle-in-cell, Advanced Methods for Space Simulations (2007) 61–76.

[16] M Li, M Merino, E Ahedo, H Tang, On electron boundary conditions in PIC plasma thruster plume simulations, Plasma Sources Sci. Technol. 28 (No. 03) (2019) 034004.

[17] M Martínez-Sánchez, J Navarro-Cavallé, E Ahedo, Electron cooling and finite potential drop in a magnetized plasma expansion, Phys. Plasmas 22 (No. 5) (2015) 053501.

[18] G Sánchez-Arriaga, J Zhou, E Ahedo, M Martínez-Sánchez, J J Ramos, Kinetic features and non-stationary electron trapping in paraxial magnetic nozzles, Plasma Sources Sci. Technol. 27 (No. 3) (2018) 035002.

[19] M Merino, J Mauriño, E Ahedo, "Kinetic electron model for plasma thruster plumes, Plasma Sources Sci. Technol. 27 (No. 3) (2018) 035013.

[20] B Korkut, Z Li, D Levin, 3-D simulation of ion thruster plumes using octree adaptive mesh refinement, IEEE Trans. Plasma Sci. 43 (No. 5) (2015) 1706–1721.

[21] C Cai, Numerical studies on plasma plume flows from a cluster of electric propulsion devices, Aero. Sci. Technol. 41 (2015) 134–143.

[22] F Taccogna, D Pagano, F Scortecci, A Garulli, Three-dimensional plume simulation of multi-channel thruster configuration, Plasma Sources Sci. Technol. 23 (No. 6) (2014) 065034.

[23] F Cichocki, A Domínguez-Vázquez, M Merino, E Ahedo, Hybrid 3D model for the interaction of plasma thruster plumes with nearby objects, Plasma Sources Sci. Technol. 26 (No. 12) (2017) 125008.

[24] F Cichocki, Analysis of the Expansion of a Plasma Thruster Plume into Vacuum, Ph.D. thesis, Universidad Carlos III de Madrid, Leganés, Spain, 2017.

[25] A Domínguez-Vázquez, F Cichocki, M Merino, P Fajardo, E Ahedo, Axisymmetric plasma plume characterization with 2D and 3D particle codes, Plasma Sources Sci. Technol. 27 (No. 10) (2018) 104009.

[26] L Garrigues, A Heron, J Adam, J Boeuf, Hybrid and particle-in-cell models of a stationary plasma thruster, Plasma Sources Sci. Technol. 9 (2000) 219.

[27] J Zhou, D Pérez-Grande, P Fajardo, E Ahedo, Numerical treatment of a magnetized electron fluid within an electromagnetic plasma thruster code, Plasma Sources Sci. Technol. 28 (No. 11) (2019) 115004.

[28] R Hockney, J Eastwood, Computer Simulation Using Particles, CRC Press, Boca Ratón, FL, 1988.

[29] M Merino, E Ahedo, Effect of the plasma-induced magnetic field on a magnetic nozzle, Plasma Sources Sci. Technol. 25 (No. 4) (2016) 045012.

[30] E Ahedo, M Merino, Two-dimensional supersonic plasma acceleration in a magnetic nozzle, Phys. Plasmas 17 (No. 7) (2010) 073501.

[31] V L Pisacane, Fundamentals of Space Systems, Oxford University Press, 2005.